

Large unconventional anomalous Hall effect far above room temperature in epitaxial Fe_3Ga_4 films

Jing Meng,¹ Huali Yang,² Yu Shen,¹ Kun Zheng,¹ Hongru Wang,¹ Yuhao Wang,¹ Keqi Xia,¹ Bocheng Yu,¹ Xiaoyan Zhu,¹ Baiqing Lv,³ Yaobo Huang,⁴ Jie Ma,⁵ Dariusz Jakub Gawryluk,⁶ Toni Shiroka,^{6,7} Zhenzhong Yang,^{1,*} Yang Xu,¹ Qingfeng Zhan,^{1,†} and Tian Shang^{1,8,‡}

¹Key Laboratory of Polar Materials and Devices (MOE), School of Physics and Electronic Science, East China Normal University, Shanghai 200241, China

²Key Laboratory of Magnetic Materials Devices, Zhejiang Province Key Laboratory of Magnetic Materials and Application Technology, Ningbo Institute of Materials Technology and Engineering, Chinese Academy of Sciences, Ningbo 315201, China

³Tsung-Dao Lee Institute, Zhangjiang Institute for Advanced Study, School of Physics and Astronomy, Shanghai Jiao Tong University, Shanghai 200240, China

⁴Shanghai Synchrotron Radiation Facility, Shanghai Advanced Research Institute, Chinese Academy of Sciences, Shanghai 201204, China

⁵Key Laboratory of Artificial Structures and Quantum Control, School of Physics and Astronomy, Shanghai Jiao Tong University, Shanghai 200240, China

⁶PSI Center for Neutron and Muon Sciences CNM, CH-5232 Villigen PSI, Switzerland

⁷Laboratorium für Festkörperphysik, ETH Zürich, CH-8093 Zürich, Switzerland

⁸Chongqing Key Laboratory of Precision Optics, Chongqing Institute of East China Normal University, Chongqing 401120, China

Abstract

Noncoplanar spin textures usually exhibit a finite scalar spin chirality (SSC) that can generate effective magnetic fields and lead to additional contributions to the Hall effect, namely topological or unconventional anomalous Hall effect (UAHE). Unlike topological spin textures (e.g., magnetic skyrmions), materials that exhibit fluctuation-driven SSC and UAHE are rare. So far, their realization has been limited to either low temperatures or high magnetic fields, both of which are unfavorable for practical applications. Identifying new materials that exhibit UAHE in a low magnetic field at room temperature is therefore essential. Here, we report the discovery of a large UAHE far above room temperature in epitaxial Fe_3Ga_4 films, where the fluctuation-driven SSC stems from the field-induced transverse-conical-spiral phase. Considering their epitaxial nature and the large UAHE stabilized at room temperature in a low magnetic field, Fe_3Ga_4 films represent an exciting, albeit rare, case of a promising candidate material for spintronic devices.

Introduction

Topological transport is a powerful yet simple method to probe the nontrivial spin textures in magnetic materials [1–3]. As such, it has become a hot topic of frontier research in condensed matter physics and materials science. A typical example of topological transport is the topological Hall effect (THE), which has been frequently observed in materials with topological spin textures, such as magnetic skyrmions [4–10]. The nontrivial topology of skyrmions implies a Berry curvature, which acts as a virtual magnetic field and gives rise to an additional transverse contribution to the Hall effect of conduction electrons, namely, to the THE [8–10]. Due to its ease of measurement, THE can be a convenient tool for the electrical read-out of spin textures in real applications [11]. Besides skyrmions, magnetic materials with noncoplanar or noncollinear spin textures may also show an unconventional anomalous Hall effect (UAHE). This appears as an addition to the conventional component that is induced by the spontaneous magnetization through the spin-orbit

interaction [12–20], challenging the necessity of topological spin textures for the THE or UAHE. Note that, in some previous work, the observed UAHE was also referred to as THE [14–18]. To avoid confusion, UAHE will be used here to refer to the magnetic materials *without* topological spin textures. As an alternative to the real-space scenario, UAHE has also been observed in systems with band structure anomalies, such as Weyl points near the Fermi level, which carry a significant Berry curvature in momentum space [21, 22]. Similar to the case of magnetic skyrmions, the scalar spin chirality (SSC) $\chi_{ijk} = \mathbf{S}_i \cdot (\mathbf{S}_j \times \mathbf{S}_k)$, which represents the solid angle subtended by adjacent spins and determines the virtual magnetic field [8–10], can also be finite in some noncoplanar magnetic materials and can be coupled to the conduction electrons to produce a UAHE.

Recent theoretical work has shown that a finite SSC can also arise dynamically from thermal spin fluctuations and persist at temperatures above the magnetic order. In such cases, the enhanced UAHE can be understood in terms of both skew scattering [23–25] and Berry curvature [26–28]. Such fluctuation- and/or thermal-driven UAHE has been experimentally realized in kagome metals [28–32], cobaltates [33], chiral magnets or ferromagnetic metals [18, 34, 35], as well as in multilayer films [36, 37]. Nevertheless, in most the above cases, the prerequisites for potential applications are not yet met. The UAHE appears either at low

* Corresponding author:
zzyang@phy.ecnu.edu.cn

† Corresponding author:
qfzhan@phy.ecnu.edu.cn

‡ Corresponding author:
tshang@phy.ecnu.edu.cn

temperatures, or at high magnetic fields, or only in a narrow temperature range close to the magnetic order. For example, Pt/Cr₂O₃ bilayers with a Cr₂O₃ thickness less than 6 nm exhibit UAHE at temperatures above the Néel order (~ 300 K) of Cr₂O₃ [37], but the unconventional anomalous Hall resistivity ρ_{xy}^U is extremely small, less than 1 n Ω cm. In this regard, it is essential to be able to identify new materials exhibiting a large ρ_{xy}^U at room temperature in zero- or a very small field.

The intermetallic Fe₃Ga₄ compound was reported to exhibit a clear UAHE in a wide temperature range below ~ 400 K [38]. Fe₃Ga₄ adopts a centrosymmetric monoclinic structure (*C2/m*), whose unit cell contains 18 Fe and 24 Ga atoms (see Fig. 1a) [39]. There are four crystallographically inequivalent Fe sites, which allows for a variety of possible nearest- and next-nearest neighbor interactions. In weak magnetic fields, Fe₃Ga₄ undergoes three magnetic transitions: a paramagnetic (PM) to ferromagnetic (FM) transition at $T_1 \sim 420$ K, a FM to antiferromagnetic (AFM) transition at $T_2 \sim 360$ K, and, finally, an AFM to the ground-state FM transition at $T_3 \sim 68$ K [38]. In the intermediate AFM state ($T_3 < T < T_2$), an incommensurate spin-density-wave (ISDW) or a helical spiral (HS) order are equally consistent with the neutron diffraction data, with the latter being more compatible with the theoretical predictions and magnetization data [40–42]. Depending on the orientation, an applied magnetic field transforms the HS order into a transverse conical spiral (TCS) or a longitudinal conical spiral (LCS) order, before entering the forced ferromagnetic (FFM) state (see Fig. 1c) [42]. Similar to the kagome metal REMn₆Sn₆ (*RE* = Sc, Y, Er) [29–31], the TCS order consists of a noncoplanar spin configuration that produces a finite χ_{ijk} via dynamic fluctuations, which could account for the observed UAHE in Fe₃Ga₄ [38]. However, the appearance of topological spin textures in Fe₃Ga₄ cannot be fully excluded. To date, the origin of the UAHE, as well as its temperature- and field evolution, remain largely unexplored. These rich magnetic phases, involving both the temperature and the magnetic field, originate from the complex magnetic interactions [41, 42]. As a consequence, the magnetic properties of Fe₃Ga₄ can be effectively tuned via external stimulus, such as, the magnetic field, doping, pressure, annealing, and dimensionality [38, 42–47].

Here, we report on the epitaxial growth of Fe₃Ga₄ films on a SrTiO₃ (STO) substrate and the systematic study of their magnetic- and transport properties. The unconventional anomalous Hall effect is shown to occur in the intermediate AFM phase, in the magnetic-field region where a series of metamagnetic transitions take place, and to cover a wide temperature range (~ 100 – 380 K). The occurrence of UAHE in Fe₃Ga₄ films is most likely attributed to the fluctuation-driven finite SSC in the noncoplanar spiral states. Besides REMn₆Sn₆, Fe₃Ga₄ is, to the best of our knowledge, the second case, where chirality fluctuations originating from the spiral phase play a key role in determining the topological transport properties. Overall, we find that the Fe₃Ga₄ film is among the most promising candidate platforms for spintronic applications.

Results

Crystal structure and characterizations of Fe₃Ga₄ films

The epitaxial nature of the sputtered Fe₃Ga₄ film was checked by x-ray diffraction (XRD) and transmission electron microscopy (TEM) measurements. Figure 1b shows a representative 2θ – ω scan of a Fe₃Ga₄ film sputtered on a (001)-oriented STO substrate. The (0k0) reflections of Fe₃Ga₄ were identified near the (00l) reflections of the STO substrate, implying that the Fe₃Ga₄ was epitaxially grown along the *b* axis. No indication of impurities or misorientations was detected in the XRD pattern. The epitaxial nature of Fe₃Ga₄ film was further confirmed by reciprocal space mapping (see Supplementary Fig. S1). The determined out-of-plane lattice parameter $b = 7.602$ Å of the film is comparable to its bulk value [38]. The cross-sectional TEM image reveals distinct interfaces between the Pt capping layer, the Fe₃Ga₄ film, and the STO substrate (see Fig. 1f), with estimated thicknesses of 6.2 and ~ 81.6 nm for the Pt layer and the Fe₃Ga₄ film, respectively. To check the crystal structure at a microscopic level, a cross sectional high-angle annular dark field-scanning transmission electron microscopy (HAADF-STEM) measurement was also performed. Figure 1g illustrates the HAADF-STEM image of Fe₃Ga₄ film viewed along the [101] direction. Clear diffraction spots in the fast Fourier transform (FFT) image (shown in the inset) suggest a well-crystallized Fe₃Ga₄ film. Both Fe and Ga atoms can be well identified in the HAADF-STEM image (see the enlarged plot in Fig. 1h), consistent with the monoclinic crystal structure of Fe₃Ga₄.

The electronic properties of the Fe₃Ga₄ film were characterized by both magnetization M and electrical resistivity ρ_{xx} measurements. The temperature-dependent magnetization $M(T)$ in Fig. 1d shows two distinct transitions at $T_C = 82$ K and $T_N = 385$ K, which correspond to the FM (T_3) and AFM (T_2) transitions of the bulk crystal [38, 40, 42], respectively. The sharp magnetic transition at T_N (with $\Delta T \sim 7$ K) confirms the high quality of the epitaxial Fe₃Ga₄ film, which is rare among the high-temperature helimagnetic films. The AFM transition is reflected also in the $\rho_{xx}(T)$ data (see dashed lines in Fig. 1e), but the FM transition is less evident (see Supplementary Fig. S2). The residual resistivity ratio (RRR ~ 17.7) is much larger than that of the bulk crystal [38, 40, 42], again indicating the high quality of our Fe₃Ga₄ film. The $M(T)$ data were collected under various magnetic fields (up to 3 T), applied both perpendicular ($H \parallel b$) and parallel ($H \parallel ac$) to the film plane (see Supplementary Fig. S3). For $H \parallel b$, as the magnetic field increases, T_C shifts to ~ 110 K for $\mu_0 H = 1$ T. In applied fields above 1 T, the FM transition evolves into a broad crossover, where the Fe moments start to be polarized along the field direction. By contrast, for $\mu_0 H = 3$ T, T_N is continuously suppressed to 362 K. The determined T_C and T_N values are summarized in the magnetic phase diagram (see below). A similar behavior was also found for $H \parallel ac$ (see details in Supplementary Fig. S3). Akin to the case of bulk crystals, also in Fe₃Ga₄ films the temperature range where the intermediate AFM phase occurs is suppressed by an external field [38, 42]. Since the highest temperature (i.e., 400 K)

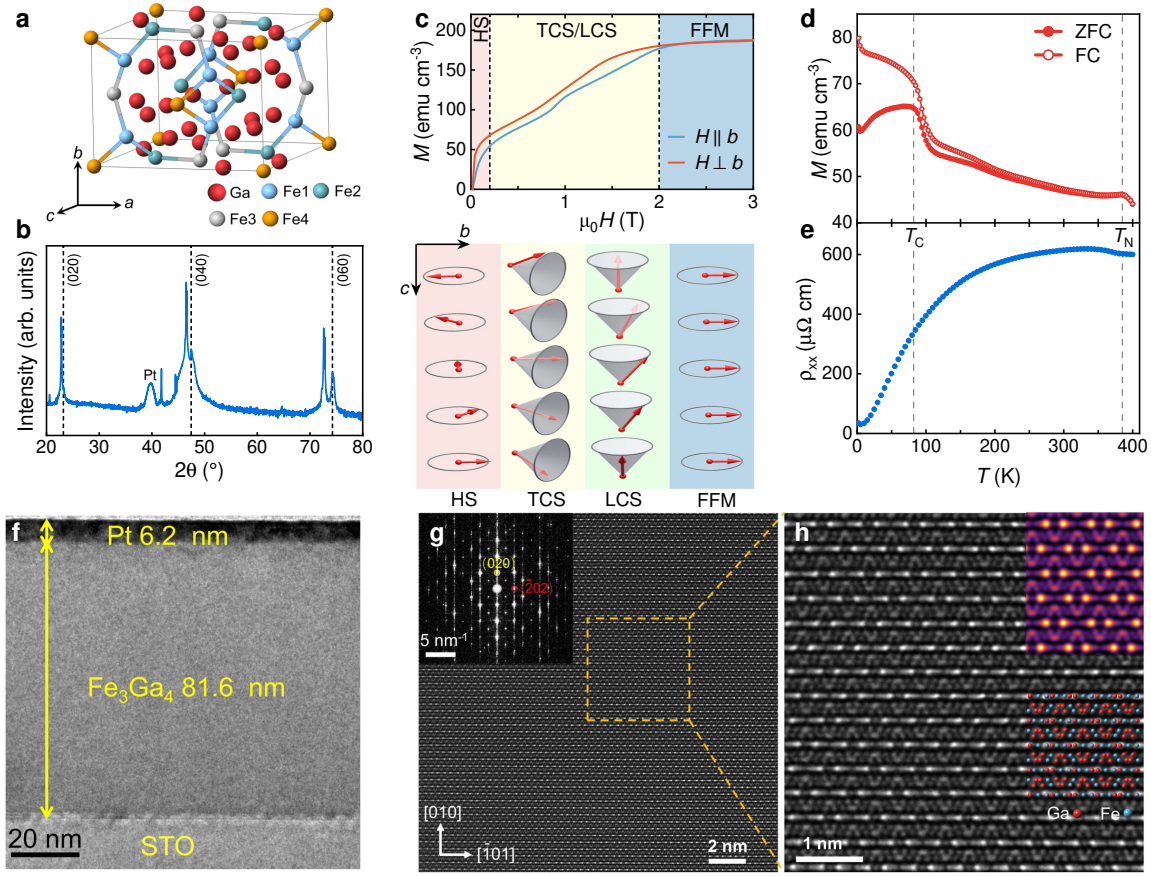


Fig. 1 Crystal structural and characterization of the epitaxial Fe_3Ga_4 film. **a** Unit-cell crystal structure of monoclinic Fe_3Ga_4 , highlighting the four nonequivalent Fe and Ga sites. Here, only the Fe atoms are shown in different colors, while all the Ga atoms are shown in red. **b** Representative XRD pattern of a Pt/ Fe_3Ga_4 /SrTiO₃ film. The series of observed (0k0) reflections confirms that the Fe_3Ga_4 film was epitaxially grown along the b axis on the (001)-oriented STO substrate. The sharp peaks at $2\theta \sim 21^\circ$ and 42° are attributed to the STO substrate (see Supplementary Fig. S1). **c** In-plane and out-of-plane field-dependent magnetization of a Fe_3Ga_4 film collected at 200 K. Various magnetic phases, including HS, TCS, LCS, and FFM order, appear as the magnetic field increases. Their magnetic structures are schematically shown below the panel. In the HS phase, the magnetic order propagates along the c axis, with the Fe moments rotating in the ab plane. For $H \parallel b$ ($H \perp b$), a metamagnetic transition from HS to TCS (LCS) was proposed. **d** Temperature-dependent zero-field-cooling (ZFC)- and field-cooling (FC) magnetization $M(T)$. **e** Temperature-dependent electrical resistivity $\rho_{xx}(T)$. The $M(T)$ was collected in a field of 0.1 T applied perpendicular to the film plane, while $\rho_{xx}(T)$ was collected in a zero-field condition. The dashed lines mark the AFM and FM transition at $T_N \sim 385$ K and $T_C \sim 82$ K, respectively. **f** TEM image of the Pt/ Fe_3Ga_4 /STO film cross-section. The Pt and Fe_3Ga_4 layers, as well as the STO substrate are clearly visible with different contrasts. **g** Atomic-resolution HAADF-STEM image and the corresponding FFT image, demonstrating the single-crystalline nature of Fe_3Ga_4 film. **h** The enlarged view of the orange-marked region in panel (g), overlaid with a simulated HAADF image and crystal models. No domain structures could be identified along the b -axis of the film. Blue and red spheres represent Fe and Ga atoms, respectively.

accessible in this work is lower than T_1 , most of the measurements were performed in the low- T FM and intermediate AFM states.

Magnetization and metamagnetic transitions

Previous work on bulk Fe_3Ga_4 crystals has shown that, in the intermediate AFM phase, the metamagnetic transitions are temperature-, field-, and orientation dependent [38, 40, 42]. Here we find that such metamagnetic transitions persist also in Fe_3Ga_4 films. After subtracting the substrate signal (see Supplementary Fig. S4), we obtain the field-dependent magnetization $M(H)$ at various temperatures, as shown in Figs. 2a,b for $H \parallel b$ and $H \parallel ac$, respectively. The magnetiza-

tion saturates when the external field exceeds the saturation field H_{c4} , whose value varies across the different magnetic phases (see phase diagram below). For $H \parallel b$, in the AFM phase, the Fe_3Ga_4 film undergoes three metamagnetic transitions as the field increases. At each transition, $M(H)$ shows a small yet clear hysteresis, which becomes less evident when approaching the FM state. For $H < H_{c4}$, as indicated by the arrows in the $M(H)$ dataset at 150 K, the three identified critical fields (determined by dM/dH in Supplementary Figs. S5 and S6) are $\mu_0 H_{c1} \sim 0.04$ T, $\mu_0 H_{c2} \sim 0.86$ T, and $\mu_0 H_{c3} \sim 1.36$ T. While in the low- T FM state, before the Fe moments are fully polarized at $H > H_{c4}$, there is also a weak metamagnetic transition at $\mu_0 H_{c1} \sim 0.08$ T (indicated by

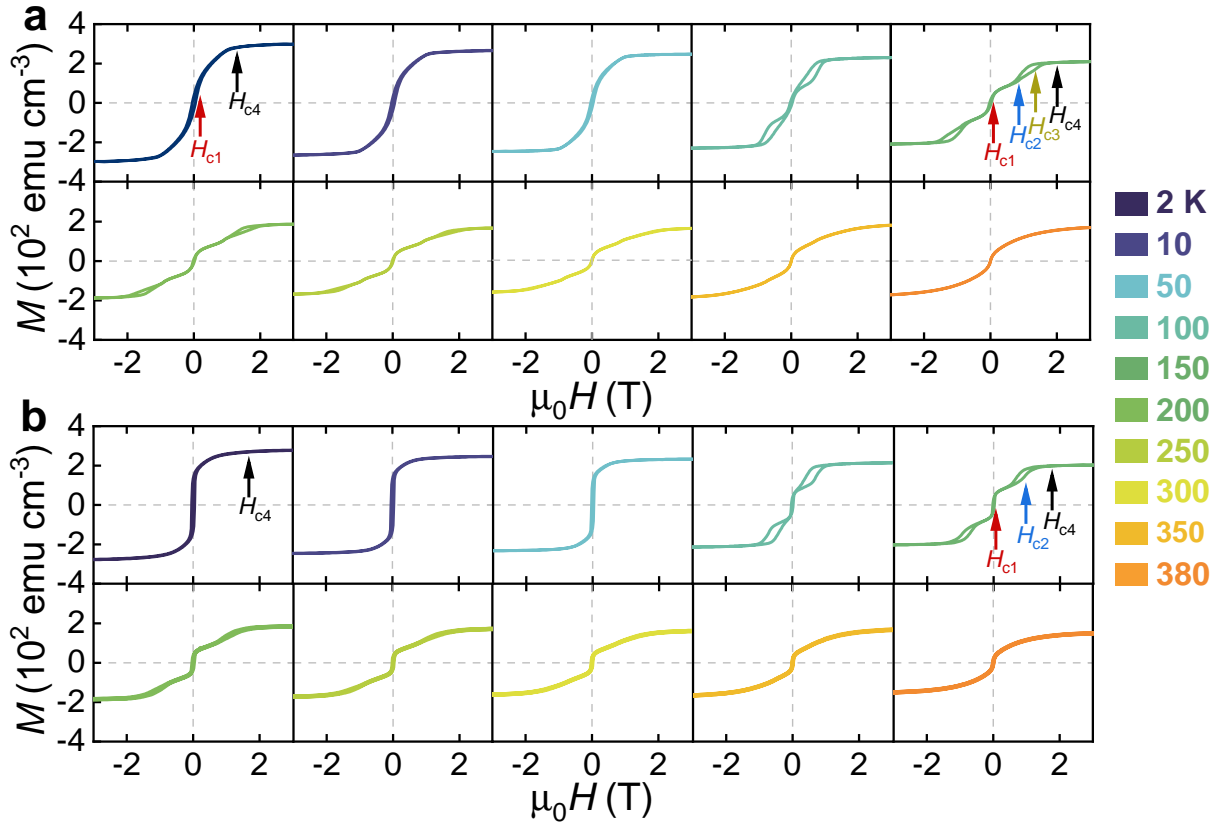


Fig. 2 Magnetization of a Fe_3Ga_4 film. **a,b** Field-dependent magnetization collected at various temperatures between 2 and 380 K with the magnetic fields applied perpendicular (i.e., $H \parallel b$) (a) and parallel to the film plane (i.e., $H \parallel ac$) (b). The signal from the STO substrate was subtracted (see Supplementary Fig. S4). The arrows mark the saturation field (H_{c4}) and the three critical fields (H_{c1} , H_{c2} , and H_{c3}), where the Fe_3Ga_4 film undergoes metamagnetic transitions. In the FM state, the metamagnetic transition was observed only for $H \parallel b$. While, in the AFM state, we observe three metamagnetic transitions for $H \parallel b$, but only two transitions for $H \parallel ac$ (see the determination of H_{c1} to H_{c4} in Supplementary Figs. S5 and S6).

an arrow in the 2-K $M(H)$ dataset), which was also present in the bulk crystal [42]. According to the neutron diffraction data, in bulk crystals in the FM state, the Fe moments are polarized along the c axis [40]. This leads to a much larger magnetization at low fields when $H \parallel c$ axis than for $H \parallel a$ or b axis [40, 42]. In a Fe_3Ga_4 film at low fields, the in-plane magnetization is much larger than the out-of-plane magnetization (see Supplementary Fig. S7), indicating that the Fe moments are aligned within the film plane (here, the ac plane). Further, although only two metamagnetic transitions could be identified for $H \parallel ac$ (see Fig. 2b and Supplementary Fig. S6), the critical fields are comparable to those obtained for $H \parallel b$. Note that, the identified metamagnetic transition at H_{c1} is most likely extrinsic and attributed to the uncompensated magnetization at the interfaces (see Supplementary Fig. S8). This assignment is also substantiated by recent neutron scattering studies on Fe_3Ga_4 bulk single crystals [48]. For this reason, H_{c1} will not be discussed further below.

Magnetoresistivity and Hall resistivity

Metamagnetic transitions appear also in the field-dependent electrical resistivity $\rho_{xx}(H)$. To perform the transport mea-

surements, the Fe_3Ga_4 film was patterned into a Hall-bar geometry (see Fig. 3a). In the FM state, there are no distinct anomalies in the $\rho_{xx}(H)$ (Fig. 3b), while both H_{c1} and H_{c4} can be identified in the $d\rho_{xx}/dH$ data (see Supplementary Fig. S9). In the AFM state, the metamagnetic transitions are obvious in the low-field region. All the critical fields, as determined from $\rho_{xx}(H)$, are highly consistent with the $M(H)$ results (see phase diagram below). Interestingly, in the low- T FM state, Fe_3Ga_4 film exhibits a giant and positive magnetoresistivity (MR), reaching $\sim 313\%$ at 2 K in a field of 9 T (see Fig. 3c and Supplementary Fig. S10). The MR decreases significantly with increasing temperature. Upon entering the intermediate AFM state, not only the sign of MR becomes negative, but also its magnitude is significantly reduced, dropping to less than 10%. A similar sign reversal of MR was observed also in bulk polycrystals [55], but it is absent in Fe_3Ga_4 single crystals [38]. Such different types of MR behavior are most likely attributed to the magnetic anisotropy of Fe_3Ga_4 . Further measurements in magnetic fields applied along different crystal orientations are desirable to clarify this issue. Numerous metamagnetic transitions are frequently observed in magnetic materials with nontrivial spin textures, such as REMn_6Sn_6 [29–31],

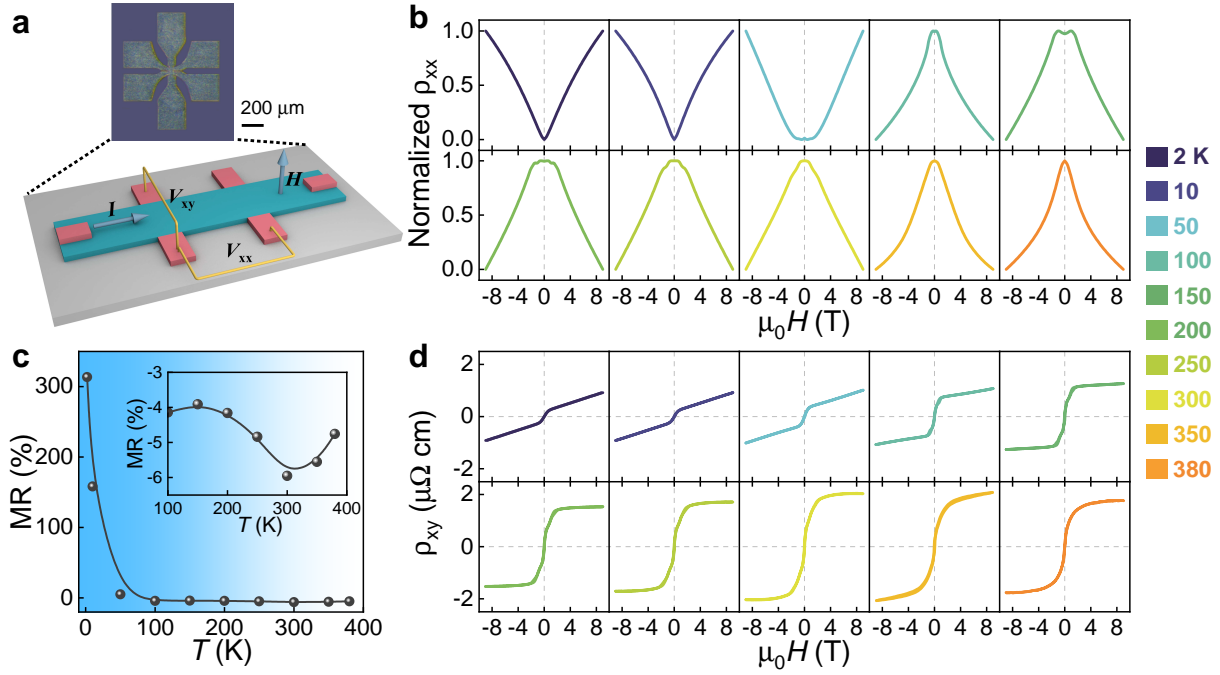


Fig. 3 Transport properties of a Fe₃Ga₄ film. **a** A representative optical image of the micro-fabricated Pt/Fe₃Ga₄/STO film with a Hall-bar geometry. The schematic drawing below the panel depicts the Hall-bar device with six electrodes and notations of longitudinal electrical resistivity ρ_{xx} ($= V_{xx}/I$) and transverse Hall resistivity ρ_{xy} ($= V_{xy}/I$) measurements. For both measurements, the dc current was applied within the film plane ($I \parallel ac$), while the magnetic field was applied perpendicular to the film plane ($H \parallel b$). **b** Field-dependent electrical resistivity $\rho_{xx}(H)$ collected at various temperatures between 2 and 380 K. To better compare the $\rho_{xx}(H)$ data at different temperatures, they were normalized to the 0–1 range. **c** Temperature dependence of the 9-T MR. The inset shows the enlarged view of MR in the AFM state. **d** Field-dependent Hall resistivity $\rho_{xy}(H)$ collected at various temperatures between 2 and 380 K.

SrCo₆O₁₁ [33], Gd₃Ru₄Al₁₂ [56], MnSi [57], and EuAl₄ [58], with the latter three known to host magnetic skyrmions. In all these materials, the Hall resistivity is usually given by the sum of an ordinary (ρ_{xy}^O), an anomalous (ρ_{xy}^A), and an unconventional anomalous (ρ_{xy}^U) Hall contribution, namely, $\rho_{xy} = \rho_{xy}^O + \rho_{xy}^A + \rho_{xy}^U$ [8–10, 12–19]. Note that, in the literature, ρ_{xy}^U is often (incorrectly) called topological Hall resistivity ρ_{xy}^T . Within the metamagnetic transitions, the above-mentioned materials exhibit a ρ_{xy}^U that results from the Berry phase acquired by the carriers when they pass through the nontrivial spin textures [8–10, 12–19]. Also here we exploit the Hall-resistivity measurements on Fe₃Ga₄ films to search for possible nontrivial spin textures (note, though, that this is only a necessary condition). In the low- T FM state, $\rho_{xy}(H)$ exhibits the typical features due to the AHE in a ferromagnet (see Fig. 3d). While in the intermediate AFM state, $\rho_{xy}(H)$ shows multiple kinks at the metamagnetic transitions at $H < H_{c4}$ (see Supplementary Fig. S11). As the magnetic field increases above H_{c4} (where the Fe moments are fully polarized), ρ_{xy}^A becomes again dominant.

Anomalous Hall effect

The obtained ρ_{xy}^A values versus temperature are summarized in Fig. 4a, which reflects the different magnetic states of a Fe₃Ga₄ film. In the low- T FM state, ρ_{xy}^A is almost temperature-independent, but it starts to increase when

entering the intermediate AFM state. As the temperature approaches the high- T FM state, ρ_{xy}^A starts to decrease again. Due to the reduced electrical resistivity (see Fig. 1e), both the electrical conductivity σ_{xx} and the anomalous Hall conductivity σ_{xy}^A are greatly enhanced in the low- T FM state (Fig. 4b,c). For instance, $\sigma_{xy}^A \sim 151 \Omega^{-1}\text{cm}^{-1}$ at 2 K is almost 30 times larger than the σ_{xy}^A values at $T > 50$ K. The temperature-dependent anomalous Hall angle $\Theta_A \equiv \tan^{-1}(\sigma_{xy}^A/\sigma_{xx})$ resembles $\sigma_{xy}^A(T)$, which exhibits clear anomalies close to T_C and T_N (Fig. 4d). Θ_A is about 0.30° at 2 K, a value comparable to that in the FM SrRuO₃ film or in the Fe₃Sn₂ kagome metal [53, 59]. In the intermediate AFM state, however, Θ_A drops by a factor of 2. To elucidate the mechanism of AHE in the Fe₃Ga₄ film, in Fig. 4e, we plot σ_{xy}^A against σ_{xx} , together with the results from the Fe₃Ga₄ bulk crystal and of those of other magnetic thin films. The scaling relation between σ_{xy}^A and σ_{xx} has been frequently studied in recent years. Generally, it can be divided into three regimes, where different mechanisms have been proposed to account for the σ_{xy}^A behavior [20, 25, 60]. In the high-conductivity regime ($\sigma_{xx} \gtrsim 5 \times 10^5 \Omega^{-1}\text{cm}^{-1}$), the extrinsic skew scattering contribution dominates AHE and $\sigma_{xy}^A \propto \sigma_{xx}$; in the good-metal regime ($3 \times 10^3 \lesssim \sigma_{xx} \lesssim 5 \times 10^5 \Omega^{-1}\text{cm}^{-1}$), σ_{xy}^A is dominated by the intrinsic Berry-phase contribution, which is approximately independent of σ_{xx} ; finally in the bad-metal

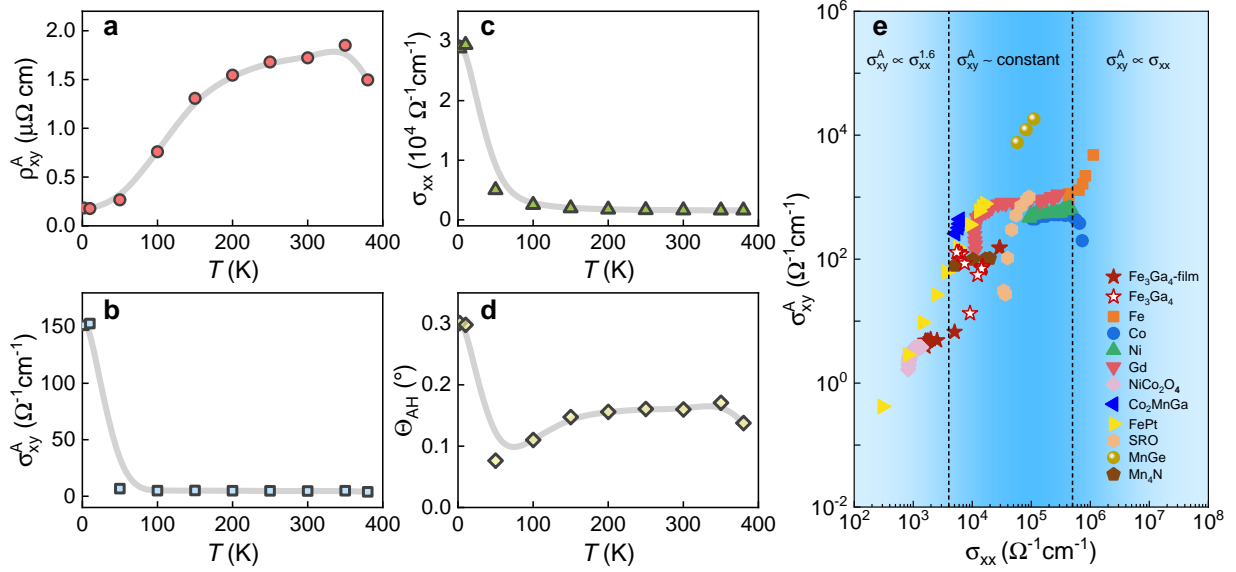


Fig. 4 Anomalous Hall effect in a Fe_3Ga_4 film. **a–d** Temperature dependence of the anomalous Hall resistivity $\rho_{xy}^A(T)$ (a), the anomalous Hall conductivity $\sigma_{xy}^A(T)$ (b), the electrical conductivity $\sigma_{xx}(T)$ (c), and the anomalous Hall angle $\Theta_A(T)$ (d) for a Fe_3Ga_4 film. The analysis of Hall-resistivity data is reported in Supplementary Figs. S10, S11, and S12. **e** σ_{xy}^A vs σ_{xx} for various types of magnetic thin films spanning different AHE regimes, from the side-jump mechanism ($\sigma_{xy}^A \propto \sigma_{xx}^{1.6}$), through the intrinsic- ($\sigma_{xy}^A \sim \text{const.}$), and skew-scattering ($\sigma_{xy}^A \propto \sigma_{xx}$) regimes. Except for the Fe_3Ga_4 film (solid stars), the data for other films were taken from Refs. [35, 49–54], while the data for the single-crystal bulk Fe_3Ga_4 (open stars) were taken from Ref. [38].

(or localized hopping) regime ($\sigma_{xx} \lesssim 3 \times 10^3 \Omega^{-1}\text{cm}^{-1}$), the extrinsic side-jump mechanism is at play and it leads to $\sigma_{xy}^A \propto \sigma_{xx}^{1.6-1.8}$. In the Fe_3Ga_4 film, for $T < 400$ K, we find that $\sigma_{xx} \sim 0.16\text{--}2.94 \times 10^4 \Omega^{-1}\text{cm}^{-1}$ (Fig. 4c) in both the good- and bad-metal regimes. Therefore, both the intrinsic Berry-phase- and the extrinsic side-jump mechanisms might account for the observed σ_{xy}^A in the Fe_3Ga_4 film. Interestingly, σ_{xy}^A in the low- T FM state is compatible with the intrinsic regime. While, in the intermediate AFM state, σ_{xy}^A is mostly in the extrinsic regime. Different from the film, σ_{xy}^A of a Fe_3Ga_4 bulk crystal is located in the intrinsic regime irrespective of its magnetic state. Such discrepancy is most likely attributed to the additional disorder/scattering at the interfaces of a Fe_3Ga_4 film, resulting in an enhanced electrical resistivity. It could be interesting to investigate Fe_3Ga_4 films with different thicknesses, where the magnetic transition temperatures and the nature of σ_{xy}^A can be tuned.

Unconventional anomalous Hall effect far above room temperature

To search for a possible unconventional anomalous contribution ρ_{xy}^U , both ρ_{xy}^O and ρ_{xy}^A were subtracted from the measured Hall resistivity ρ_{xy} . While $\rho_{xy}^O (= R_0 H)$ is proportional to the applied magnetic field, $\rho_{xy}^A (= R_S M)$ is mostly determined by the magnetization (see details in the Materials and Methods Section). In real materials, ρ_{xy}^A depends on the mechanism at play, i.e., whether it is intrinsic, side-jump, skew scattering, or an intricate combination thereof [20, 25, 60]. The different contributions to the Hall

resistivity in the intermediate AFM state (e.g., at 200 K) and FM state of a Fe_3Ga_4 film are shown in Fig. 5a and Fig. 5b, respectively, with the other temperatures showing similar results (see Supplementary Fig. S11). Here, we use ρ_{xx}^2 to extract ρ_{xy}^A by using the relation $\rho_{xy}^A = S_H \rho_{xx}^2 M$ in the AFM state, where S_H is a field-independent scaling factor. The obtained R_0 and R_S are summarized in Supplementary Fig. S12. We note that the use of $S_H \rho_{xx}^2$, $S_H \rho_{xx}$, or simply S_H for R_S leads to a comparable unconventional anomalous contribution $\rho_{xy}^U(H)$ (see Supplementary Fig. S13). After subtracting $\rho_{xy}^O(H)$ and $\rho_{xy}^A(H)$, the extracted unconventional anomalous contributions $\rho_{xy}^U(H)$ at various temperatures are shown in Fig. 5c, as well as presented as a background in the magnetic phase diagram in Fig. 5d. The hump-like anomaly in $\rho_{xy}^U(H)$ resembles the typical feature of UAHE caused by non-trivial spin textures [8–10, 12–19]. ρ_{xy}^U is almost absent in the low- T FM state. While in the intermediate AFM state, in the field range between H_{c1} and H_{c3} (marked as AFM1 and AFM2), where Fe_3Ga_4 undergoes metamagnetic transitions, ρ_{xy}^U is particularly evident, and it becomes almost invisible at $H > H_{c3}$ (i.e., AFM3 and FFM phases). The field-dependent ρ_{xy}^U increases sharply and peaks at $\mu_0 H \sim 0.4$ T below the room temperature (Fig. 5c). Such a peak moves to slightly lower fields when the temperature increases. ρ_{xy}^U reaches a maximum value of $\sim 0.36 \mu\Omega\text{cm}$ at 350 K in a field of $\mu_0 H = 0.35$ T. We found that the Fe_3Ga_4 film exhibits a much larger ρ_{xy}^U than other multilayer systems, which host topological spin textures at room temperature [61–65].

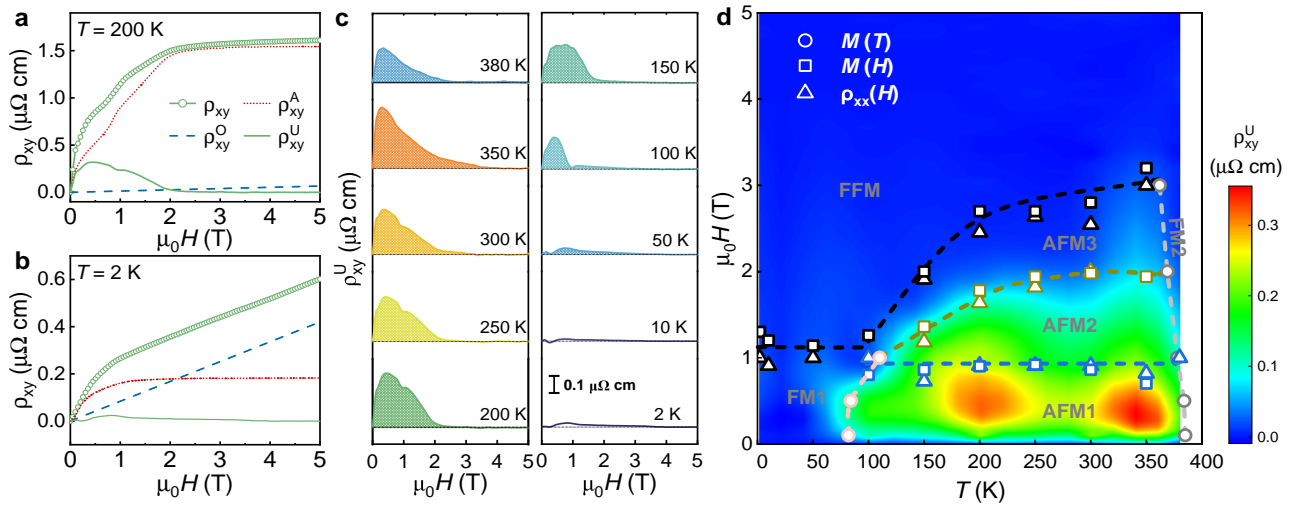


Fig. 5 Unconventional Hall effect and magnetic phase diagram of a Fe_3Ga_4 film. **a-b** Analysis of the field-dependent Hall resistivity $\rho_{xy}(H)$ collected at 200 K (a) and 2 K (b) for a Fe_3Ga_4 film. Dashed, dotted, and solid lines represent the ordinary (ρ_{xy}^O), anomalous (ρ_{xy}^A), and unconventional anomalous (ρ_{xy}^U) contributions to the Hall resistivity, respectively. The $\rho_{xy}(H)$ curves at other temperatures were analyzed using the same procedure, (see Supplementary Fig. S11). **c** Extracted field-dependent unconventional anomalous Hall resistivity $\rho_{xy}^U(H)$ at different temperatures between 2 and 380 K. Here, only the data collected by increasing the magnetic field are plotted. No visible ρ_{xy}^U could be identified in the low- T FM state. **d** Magnetic phase diagram of a Fe_3Ga_4 film with $H \parallel b$ (i.e., H perpendicular to the film plane), as obtained from the $M(T)$, $M(H)$, and $\rho_{xx}(H)$ datasets (see Supplementary Figs. S3, S5, and S9). The background color represents the magnitude of ρ_{xy}^U at various temperatures. AFM1, AFM2, and AFM3 denote the three different antiferromagnetic phases, while FM1 and FM2 are the two ferromagnetic phases. FFM stands for the forced ferromagnetic phase. Dashed lines in panel (d) are guides to the eyes.

Discussion

After comprehensively characterizing the magnetization and electrical transport of the Fe_3Ga_4 films, its magnetic phase diagram could be established (Fig. 5d and Supplementary Fig. S16). Similar to the bulk crystal [38, 42], the Fe_3Ga_4 film also exhibits an intermediate AFM phase intercalated by a low- T (FM1) and a high- T FM phase (FM2). For $H \parallel b$, the Fe_3Ga_4 film undergoes two metamagnetic transitions before being fully polarized in the AFM phase at higher fields. While, for $H \parallel ac$, only one metamagnetic transition can be identified. As the magnetic field increases, ρ_{xy}^U increases sharply and peaks at $\mu_0 H \sim 0.5$ T. Further, as the field is swept across H_{c2} , ρ_{xy}^U starts to decrease and it vanishes at $H > H_{c3}$. Clearly, the UAHE appears only in the AFM1 and AFM2 phases (i.e., $H < H_{c3}$) and across a very wide temperature range, i.e., ~ 100 –380 K. The above features resemble those typical of materials with nontrivial spin textures [19, 29–31, 33, 56–58], where UAHE or THE is attributed to the SSC, albeit mostly limited to much lower temperatures. Bulk Fe_3Ga_4 crystal possesses an HS order with a complex competition between FM and AFM interactions [40–42], which also generates multiple metamagnetic transitions that are tuned by both magnetic field and temperature. The HS order evolves into an LCS- or a TCS noncoplanar order when applying a magnetic field parallel or perpendicular to the c axis, respectively [41, 42]. In the case of Fe_3Ga_4 films, for $H \parallel b$ (see magnetic phase diagram in Fig. 5d), the UAHE appears only in the AFM1 and AFM2 phases but is absent in the AFM3 phase. Thus, the

former two phases are most likely to host a TCS state, while the latter is more likely to consist of a fan-like magnetic state, similar to that in $\text{RE Mn}_6\text{Sn}_6$ ($\text{RE} = \text{Sc}, \text{Y}$) kagome metals [29, 31].

Now we discuss the possible mechanisms for the observed robust UAHE in Fe_3Ga_4 films. The THE has been found in a centrosymmetric breathing kagome lattice $\text{Gd}_3\text{Ru}_4\text{Al}_{12}$ [56] where, in the field range ~ 1 –2 T, a skyrmion lattice forms over the TCS phase below ~ 10 K favored by thermal fluctuations. In the case of Fe_3Ga_4 films, the topological spin textures might also develop from its noncoplanar magnetic order. Fe_3Ga_4 films show a strong magnetic anisotropy (see Supplementary Fig. S7), which can compete with its complex magnetic interactions and result in topological spin textures. Such a mechanism has been proposed to explain the formation of magnetic skyrmions in centrosymmetric GdRu_2Si_2 [66]. Similar to the $\text{Gd}_3\text{Ru}_4\text{Al}_{12}$ and GdRu_2Si_2 , the Dzyaloshinskii-Moriya interaction (DMI) is also absent in the centrosymmetric Fe_3Ga_4 bulk crystal. However, DMI could be present in epitaxial Fe_3Ga_4 films. Considering the rather thick Fe_3Ga_4 films (~ 81.6 nm) investigated here, the effects of interfacial DMI at the Pt/ Fe_3Ga_4 and Fe_3Ga_4 /STO interfaces should be excluded. In general, to understand the role of interfacial DMI and its effects on the topological transport properties, future studies of Fe_3Ga_4 films with different thickness (ideally less than 20 nm) and different capping layers are highly desirable. However, the in-plane (i.e., ac -plane) lattice and angle mismatches between Fe_3Ga_4 film and STO substrate can cause inhomogeneous lattice distortions and

domain structures (with a typical size of ~ 200 nm) in the film plane, both of which can locally break the inversion symmetry and thus, introduce a local DMI.

To gain more insight into the nature of observed UAHE, as well as to search for possible topological spin textures in Fe_3Ga_4 films, preliminary magnetic force microscopy (MFM) measurements were carried out at room temperature. MFM is a commonly used technique for imaging nontrivial spin textures in real space as a complementary measurement to the topological transport properties [61, 64]. The MFM measurements reveal distinct bubble-like magnetic domains, whose density increases progressively with the magnetic field (see Supplementary Fig. S17). Interestingly, at room temperature, the estimated density $n_{\text{mb}}(H)$ of magnetic bubbles scales almost linearly with $\rho_{\text{xy}}^{\text{U}}(H)$, which provides possible evidence that the appearance of topological spin textures could be at the origin of UAHE in the Fe_3Ga_4 films. In the adiabatic approximation, that is, by assuming a strong coupling of the charge with a local spin, the topological Hall resistivity $\rho_{\text{xy}}^{\text{T}}$ is generally expressed as $\rho_{\text{xy}}^{\text{T}} = PR_0B_{\text{eff}}$. Here, P is the spin polarization of charge carriers, R_0 is the effective density of charge contributing to the THE, usually taken as the ordinary Hall coefficient, and B_{eff} is the effective (emergent) magnetic field experienced by carriers due to the Berry phase they accumulate while traversing the topological spin textures, e.g., skyrmions [8, 64, 67]. The B_{eff} is defined as $B_{\text{eff}} = n_{\text{sk}}\Phi_0$, where n_{sk} is the skyrmion density and Φ_0 the magnetic flux quantum. By assuming a spin polarization $P = 0.1$ – 1 and using the n_{mq} estimated from the MFM images, the calculated $\rho_{\text{xy}}^{\text{T}}$ is about 0.1 – $1 \times 10^{-4} \mu\Omega \text{ cm}$, which is thousand times smaller than the observed $\rho_{\text{xy}}^{\text{U}} = 0.26 \mu\Omega \text{ cm}$ at 300 K. Such a significant discrepancy unambiguously excludes a key role of topological spin textures in determining the observed UAHE in Fe_3Ga_4 films. If any $\rho_{\text{xy}}^{\text{T}}$ exists, it should represent only a minor contribution to the observed total $\rho_{\text{xy}}^{\text{U}}$. However, the appearance of topological spin textures cannot be fully excluded, considering the linear scaling of $\rho_{\text{xy}}^{\text{U}}(H)$ with $n_{\text{mb}}(H)$ previously observed also in other skyrmion-hosting multilayers [64, 68] and oxide thin films [69, 70]. Thus, it could be interesting to further investigate the possible nontrivial spin textures in Fe_3Ga_4 films via other real-space imaging techniques [68, 71, 72].

As an alternative, the fluctuation-driven SSC is most likely the mechanism for UAHE in Fe_3Ga_4 films. Such a mechanism has been frequently used to explain the UAHE in different type of materials [18, 28–37]. Among these, the REMn_6Sn_6 family shows a similar picture to Fe_3Ga_4 films, where the $3d$ magnetic moments of Mn or Fe undergo transitions from a helical spiral to a transverse-conical spiral and, finally, to a fan-like state before entering the forced ferromagnetic state [29–31, 42]. In both REMn_6Sn_6 and Fe_3Ga_4 , the UAHE appears solely in the TCS phase, which belongs to one of the noncoplanar spin structures that can produce a finite SSC with the assistance of dynamic fluctuations or in presence of DMI [29]. Indeed, recently, such a fluctuation-driven mechanism has been verified in Fe_3Ga_4 bulk crystals and shown to quantitatively reproduce the observed UAHE [38, 41].

Considering that both epitaxial Fe_3Ga_4 films and bulk crystal show comparable magnetic phase diagrams and UAHE, the fluctuation-driven mechanism should be at the origin of the observed UAHE in the film as well. Our work also demonstrates that, in view of the relatively large electrical conductivity (see Fig. 4e), the large UAHE of the Fe_3Ga_4 films is mostly related to the Berry curvature rather than to the skew scattering mechanism. Finally, we compare the Fe_3Ga_4 films with other materials that exhibit a fluctuation-driven UAHE (see Supplementary Table S1). For instance, in the REMn_6Sn_6 family [29–31], the UAHE appears also in a wide temperature range (~ 100 – 300 K) with a maximum $\rho_{\text{xy}}^{\text{U}}$ reaching ~ 1 – $2 \mu\Omega \text{ cm}$. However, the critical field required to reach the maximum $\rho_{\text{xy}}^{\text{U}}$ is relatively large (about 1 T). The LaMn_2Ge_2 ferromagnet also shows results comparable to those of REMn_6Sn_6 [18]. In the case of thin films, although the critical field is relatively small, the UAHE appears either at low temperatures (e.g., at ~ 130 K in SrRuO_3) [36], or in a narrow temperature range close to the magnetic order (e.g., in $\text{Pt/Cr}_2\text{O}_3$ films) [37]. In addition, the $\rho_{\text{xy}}^{\text{U}}$ is extremely small in these films, much less than $0.1 \mu\Omega \text{ cm}$. The epitaxial Fe_3Ga_4 film is clearly superior to the above mentioned materials. Its UAHE is present over a wide temperature range (~ 100 – 380 K), with a $\rho_{\text{xy}}^{\text{U}}$ up to $0.4 \mu\Omega \text{ cm}$ achieved under a magnetic field of less than 0.4 T. Note that the uncompensated magnetization at the interfaces has little influence on the extracted temperature- and field-dependent $\rho_{\text{xy}}^{\text{U}}$ in the Fe_3Ga_4 film. Although the magnitude of $\rho_{\text{xy}}^{\text{U}}$ changes slightly when considering the interface magnetization, the main features and the extracted parameters are quite robust (see Supplementary Figs. S14 and S15).

In summary, by systematic measurements of electrical transport and magnetization, we could establish the magnetic phase diagram of epitaxial Fe_3Ga_4 films. Similar to the bulk crystal, Fe_3Ga_4 films exhibit a rich magnetic phase diagram, including FM and AFM orders, as well as multiple metamagnetic transitions. The UAHE appears in the intermediate AFM state, covering a very wide temperature range, from 100 to 380 K. Such an AFM state is consistent with the TCS phase observed in the Fe_3Ga_4 bulk crystal. Therefore, we believe that the fluctuation-driven finite SSC in the TCS phase promotes a large UAHE in Fe_3Ga_4 films. Further advantages include the possibility of epitaxial growth of a Fe_3Ga_4 film on single-crystalline substrates or the high tunability of its topological properties through strain engineering or piezoelectric effect. Finally, the large UAHE achieved well above room temperature and in small magnetic fields makes the Fe_3Ga_4 film a very promising platform for spintronic applications.

Note added. After the present manuscript was submitted, a related work by Baral et al. [48] appeared, in which bulk Fe_3Ga_4 crystals were studied via neutron scattering under various magnetic fields. In this study, a nontrivial spin texture was also proposed to occur in the magnetic phase where $\rho_{\text{xy}}^{\text{U}}$ reaches its maximum value.

Methods

Thin-film growth

The lattice parameters of the bulk Fe_3Ga_4 crystal are $a = 10.0979 \text{ \AA}$, $b = 7.6670 \text{ \AA}$, and $c = 7.8733 \text{ \AA}$ [38]. Therefore, an SrTiO_3 substrate matches very well the Fe_3Ga_4 lattice, since its lattice parameter ($a = 3.860 \text{ \AA}$) is almost identical to half of the Fe_3Ga_4 b axis. Fe_3Ga_4 films were epitaxially grown on (001)-oriented STO substrates in an ultra-high vacuum (10^{-8} Torr) magnetron sputtering system. The STO substrate was preliminarily annealed in vacuum for 1 h at 600°C , so as to remove the surface contaminants. Subsequently, a Fe_3Ga_4 film was sputtered from the alloy target in a 3 mTorr argon atmosphere at 600°C . Then the film was annealed *in situ* for extra 2 hours to improve its crystallinity. Finally, a Pt capping layer was sputtered on top of the Fe_3Ga_4 layer in a 2 mTorr argon atmosphere at room temperature. The thickness of each layer was calibrated by means of x-ray reflectivity (XRR).

Structural characterization

The crystal structure and epitaxial nature of the Fe_3Ga_4 films were characterized by room-temperature x-ray diffraction measurements. The 2θ - ω scan, XRR, and RSM were collected using a PANalytical X'Pert Pro x-ray diffractometer with $\text{Cu K}\alpha$ radiation ($\lambda = 1.5418 \text{ \AA}$). The cross-sectional transmission electron microscopy (TEM) sample was prepared using a focused ion beam and was measured by scanning electron microscope (Helios G4 UX, Thermo Fisher). Atomic resolution high-angle annular dark field (HAADF) scanning transmission electron microscopy (STEM) observations were performed using a 300 kV spherical aberration (Cs)-corrected STEM (JEM-ARM300F, JEOL). The convergence angle was 28 mrad and the angular range of collected electrons for the HAADF-STEM imaging was 64–180 mrad. The HAADF-STEM image was simulated using the Dr. Probe software package [73].

Magnetization measurement

The temperature- $M(T)$ and field-dependent $M(H)$ magnetizations were measured using a Quantum Design magnetic property measurement system. A Fe_3Ga_4 film with typical dimensions of $1.6 \times 1.8 \text{ mm}^2$ was used for the magnetization measurements. The $M(T)$ data in various magnetic fields were collected using a zero-field-cooling protocol. While for the $M(H)$ data, the full magnetic hysteresis loops were collected. For both measurements, the magnetic fields were applied both along the b axis (i.e., perpendicular to the film plane) and within the ac plane (i.e., parallel to the film plane). The signal from the STO substrate was subtracted from the measured $M(H)$ (see Supplementary Fig. S4). While for the $M(T)$, considering that the STO substrate exhibits an almost temperature-independent magnetization, such subtraction was not necessary and the data shown in fig. S3 refer to the measured $M(T)$.

Electrical transport measurement

For the transport measurements, the Fe_3Ga_4 film was patterned into a Hall-bar geometry (central area: $100 \mu\text{m} \times 20 \mu\text{m}$; electrodes: $20 \mu\text{m} \times 20 \mu\text{m}$) by photolithography

and Ar-ion-beam etching techniques (see Fig. 3a). The transport measurements were performed in a Quantum Design physical property measurement system using a standard four-probe method. For the resistivity measurements, the electric current was applied in the film plane, while the magnetic field was applied perpendicular to the film plane. To avoid spurious resistivity contributions due to misaligned Hall probes, all the resistivity measurements were performed in both positive- and negative magnetic fields. Then, in the case of the Hall resistivity ρ_{xy} , the spurious longitudinal contribution was removed by an antisymmetrization procedure, i.e., $\rho_{xy}(H) = [\rho_{xy}(H) - \rho_{xy}(-H)]/2$. Whereas in the case of the longitudinal electrical resistivity ρ_{xx} , the spurious transverse contribution was removed by a symmetrization procedure, i.e., $\rho_{xx}(H) = [\rho_{xx}(H) + \rho_{xx}(-H)]/2$.

Analysis of Hall resistivity

In magnetic materials with topologically chiral spin textures, the Hall resistivity is typically written in the form of $\rho_{xy} = \rho_{xy}^O + \rho_{xy}^A + \rho_{xy}^U$, where the three terms represent the contributions from the ordinary, the anomalous, and the THE, respectively. The ordinary Hall term $\rho_{xy}^O (= R_0 H)$ is proportional to the applied magnetic field, the anomalous Hall term $\rho_{xy}^A (= R_S M)$ is mostly determined by the magnetization. Here, R_0 is the ordinary Hall constant (that is closely related to the sign and density of the conducting carriers) and R_S is proportional to ρ_{xx}^2 or ρ_{xx} or a constant. In the FM state, we simply use $M(H)$ to obtain ρ_{xy}^A from $\rho_{xy}^A = R_S M$, where R_S is a field-independent scaling factor. In the AFM state, since the intrinsic mechanism is thought to describe the Fe_3Ga_4 film in the resistivity range, the relation $R_S = S_H \rho_{xx}^2(H)$ was used to interpret the ρ_{xy}^A term, where S_H is the intrinsic AHE coefficient, a parameter with a close connection to the electronic structure. We also note that the use of $M(H)$ or $\rho_{xx}^2 M(H)$ for ρ_{xy}^A in the full temperature range leads to comparable ρ_{xy}^U values (see Supplementary Fig. S13). After subtracting both the ordinary $\rho_{xy}^O(H)$ and the anomalous term $\rho_{xy}^A(H)$ from the measured Hall resistivity $\rho_{xy}(H)$, the unconventional anomalous Hall term $\rho_{xy}^U(H)$ was obtained. Further, to understand the nature of AHE in Fe_3Ga_4 films, the electrical- and Hall conductivity were calculated using the expressions $\sigma_{xx} = \rho_{xx}/(\rho_{xx}^2 + \rho_{xy}^2)$ and $\sigma_{xy} = \rho_{xy}/(\rho_{xx}^2 + \rho_{xy}^2)$, respectively. The anomalous Hall conductivity instead was calculated according to $\sigma_{xy}^A = \rho_{xy}^A/[(\rho_{xy}^A)^2 + \rho_{xx}^2]$, where ρ_{xx} is the zero-field electrical resistivity.

Magnetic force microscopy

Magnetic force microscopy experiments were carried out in a Bruker Icon atomic force microscope using commercially available magnetic tips (Bruker, MESP-V2) with a typical spring constant of 2.8 N/m . The MFM images were acquired using the lift mode, where the tip was lifted about 60 nm above the sample surface. In these MFM measurements, the phase shift of the cantilever is proportional to the out-of-plane stray-field gradient. The NanoScope Analysis software

allowed us to binarize all the images at the same threshold starting from the same vertical scale. The particle analysis module of this software was utilized to count the number of bubbles. The magnetic field was first set to zero before acquiring the MFM images at the target magnetic fields.

Data availability

All data needed to evaluate the conclusions in the paper are present in the paper and the Supplementary Information file. All raw data related to the current study are available from the corresponding authors upon request.

References

1. Nagaosa, N., Morimoto, T. & Tokura, Y. Transport, magnetic and optical properties of Weyl materials. *Nat. Rev. Mater.* **5**, 621–636 (2020).
2. Wang, H., Dai, Y., Chow, G.-M. & Chen, J. Topological Hall transport: Materials, mechanisms and potential applications. *Prog. Mater. Sci.* **130**, 100971 (2022).
3. Liu, Z. *et al.* Topological thermal transport. *Nat. Rev. Phys.* **6**, 554–565 (2024).
4. Fert, A., Cros, V. & Sampaio, J. Skyrmions on the track. *Nat. Nanotechnol.* **8**, 152–156 (2013).
5. Kanazawa, N., Seki, S. & Tokura, Y. Noncentrosymmetric magnets hosting magnetic skyrmions. *Adv. Mater.* **29**, 1603227 (2017).
6. Reichhardt, C., Reichhardt, C. & Milošević, M. Statics and dynamics of skyrmions interacting with disorder and nanostructures. *Rev. Mod. Phys.* **94**, 035005 (2022).
7. Fert, A., Reyren, N. & Cros, V. Magnetic skyrmions: advances in physics and potential applications. *Nat. Rev. Mater.* **2**, 17031 (2017).
8. Nagaosa, N. & Tokura, Y. Topological properties and dynamics of magnetic skyrmions. *Nat. Nanotechnol.* **8**, 899–911 (2013).
9. Jiang, W. *et al.* Skyrmions in magnetic multilayers. *Phys. Rep.* **704**, 1–49 (2017).
10. Tokura, Y. & Kanazawa, N. Magnetic skyrmion materials. *Chem. Rev.* **121**, 2857–2897 (2021).
11. Maccariello, D. *et al.* Electrical detection of single magnetic skyrmions in metallic multilayers at room temperature. *Nat. Nanotechnol.* **13**, 233–237 (2018).
12. Taguchi, Y., Oohara, Y., Yoshizawa, H., Nagaosa, N. & Tokura, Y. Spin chirality, Berry phase, and anomalous Hall effect in a frustrated ferromagnet. *Science* **291**, 2573–2576 (2001).
13. Machida, Y. *et al.* Unconventional anomalous Hall effect enhanced by a noncoplanar spin texture in the frustrated Kondo lattice $\text{Pr}_2\text{Ir}_2\text{O}_7$. *Phys. Rev. Lett.* **98**, 057203 (2007).
14. Ueda, K. *et al.* Topological Hall effect in pyrochlore lattice with varying density of spin chirality. *Phys. Rev. Lett.* **108**, 156601 (2012).
15. O'Neill, C. D., Wills, A. S. & Huxley, A. D. Possible topological contribution to the anomalous Hall effect of the noncollinear ferromagnet Fe_3Sn_2 . *Phys. Rev. B* **100**, 174420 (2019).
16. Giri, B. *et al.* Robust topological Hall effect driven by tunable noncoplanar magnetic state in Mn-Pt-In inverse tetragonal Heusler alloys. *Phys. Rev. B* **102**, 014449 (2020).
17. Rout, P. K., Madduri, P. V. P., Manna, S. K. & Nayak, A. K. Field-induced topological Hall effect in the noncoplanar triangular antiferromagnetic geometry of Mn_3Sn . *Phys. Rev. B* **99**, 094430 (2019).
18. Roychowdhury, S. *et al.* Giant room-temperature topological Hall effect in a square-net ferromagnet LaMn_2Ge_2 . *Adv. Mater.* **36**, 2305916 (2024).
19. Skorupskii, G. *et al.* Designing giant Hall response in layered topological semimetals. *Nat. Commun.* **15**, 10112 (2024).
20. Nagaosa, N., Sinova, J., Onoda, S., MacDonald, A. H. & Ong, N. P. Anomalous Hall effect. *Rev. Mod. Phys.* **82**, 1539–1592 (2010).
21. Nakatsuji, S., Kiyohara, N. & Higo, T. Large anomalous Hall effect in a non-collinear antiferromagnet at room temperature. *Nature* **527**, 212–215 (2015).
22. Liang, T. *et al.* Ultrahigh mobility and giant magnetoresistance in the Dirac semimetal Cd_3As_2 . *Nat. Mater.* **14**, 280–284 (2015).
23. Ishizuka, H. & Nagaosa, N. Spin chirality induced skew scattering and anomalous Hall effect in chiral magnets. *Sci. Adv.* **4**, eaap9962 (2018).
24. Kato, Y. & Ishizuka, H. Colossal enhancement of spin-chirality-related Hall effect by thermal fluctuation. *Phys. Rev. Appl.* **12**, 021001 (2019).
25. Yang, S.-Y. *et al.* Giant, unconventional anomalous Hall effect in the metallic frustrated magnet candidate, KV_3Sb_5 . *Sci. Adv.* **6**, eabb6003 (2020).
26. Hou, W.-T., Yu, J.-X., Daly, M. & Zang, J. Thermally driven topology in chiral magnets. *Phys. Rev. B* **96**, 140403 (2017).
27. Lu, Y., Guo, X., Koval, V. & Jia, C. Topological thermal Hall effect driven by spin-chirality fluctuations in frustrated antiferromagnets. *Phys. Rev. B* **99**, 054409 (2019).
28. Kolincio, K. K. *et al.* Large Hall and Nernst responses from thermally induced spin chirality in a spin-trimer ferromagnet. *Proc. Natl. Acad. Sci.* **118**, e2023588118 (2021).
29. Ghimire, N. J. *et al.* Competing magnetic phases and fluctuation-driven scalar spin chirality in the kagome metal YMn_6Sn_6 . *Sci. Adv.* **6**, eabe2680 (2020).
30. Fruhling, K. *et al.* Topological Hall effect induced by chiral fluctuations in ErMn_6Sn_6 . *Phys. Rev. Mater.* **8**, 094411 (2024).
31. Zhang, H. *et al.* Magnetic field-induced nontrivial spin chirality and large topological Hall effect in kagome magnet ScMn_6Sn_6 . *Appl. Phys. Lett.* **121**, 202401 (2022).
32. Kolincio, K. K. *et al.* Kagome lattice promotes chiral spin fluctuations. *Phys. Rev. Lett.* **130**, 136701 (2023).
33. Abe, N. *et al.* Large anomalous Hall effect in spin fluctuating devil's staircase. *npj Quant. Mater.* **9**, 41 (2024).
34. Gong, G. *et al.* Large topological Hall effect near room temperature in noncollinear ferromagnet LaMn_2Ge_2 single crystal. *Phys. Rev. Mater.* **5**, 034405 (2021).
35. Fujishiro, Y. *et al.* Giant anomalous Hall effect from spin-chirality scattering in a chiral magnet. *Nat. Commun.* **12**, 317 (2021).
36. Wang, W. *et al.* Spin chirality fluctuation in two-dimensional ferromagnets with perpendicular magnetic anisotropy. *Nat. Mater.* **18**, 1054–1059 (2019).
37. Cheng, Y., Yu, S., Zhu, M., Hwang, J. & Yang, F. Evidence of the topological Hall effect in Pt/antiferromagnetic insulator bilayers. *Phys. Rev. Lett.* **123**, 237206 (2019).
38. Mendez, J. H. *et al.* Competing magnetic states, disorder, and the magnetic character of Fe_3Ga_4 . *Phys. Rev. B* **91**, 144409 (2015).
39. Kawamiya, N. & Adachi, K. Magnetic and Mössbauer studies of metamagnetic Fe_3Ga_4 . *J. Phys. Soc. Jpn.* **55**, 630–634 (1986).
40. Wu, Y. *et al.* Spin density wave instability in a ferromagnet. *Sci. Rep.* **8**, 5225 (2018).
41. Afshar, M. & Mazin, I. I. Spin spiral and topological Hall effect in Fe_3Ga_4 . *Phys. Rev. B* **104**, 094418 (2021).
42. Wilfong, B. *et al.* Helical spin ordering in room-temperature metallic antiferromagnet Fe_3Ga_4 . *J. Alloys. Compd.* **917**, 165532 (2022).

43. Wilfong, B. *et al.* Altering the magnetic ordering of Fe_3Ga_4 via thermal annealing and hydrostatic pressure. *J. Alloys. Compd.* **894**, 162421 (2022).
44. Al-Kanani, H. & Booth, J. Magnetic phase transitions in $(\text{Fe}_{1-x}\text{T}_x)_3\text{Ga}_4$ alloys. *Physica B* **246–247**, 537–540 (1998).
45. Kawamiya, N. & Adachi, K. Magnetic phase changes in $(\text{Fe}_{1-x}\text{Co}_x)_3\text{Ga}_4$. *J. Magn. Magn. Mater.* **54–57**, 941–942 (1986).
46. Wilfong, B. *et al.* The effect of vanadium substitution on the structural and magnetic properties of $(\text{Fe}_{1-x}\text{V}_x)_3\text{Ga}_4$. *J. Magn. Magn. Mater.* **563**, 169964 (2022).
47. Moura, K. O. *et al.* Dimensionality tuning of the electronic structure in Fe_3Ga_4 magnetic materials. *Sci. Rep.* **6**, 28364 (2016).
48. Baral, P. R. *et al.* Fluctuation-driven topological Hall effect in room-temperature itinerant helimagnet Fe_3Ga_4 . *arXiv e-prints* arXiv:2502.13343 (2025).
49. Miyasato, T. *et al.* Crossover behavior of the anomalous Hall effect and anomalous Nernst in itinerant ferromagnets. *Phys. Rev. Lett.* **99**, 086602 (2007).
50. Kan, D., Xie, L. & Shimakawa, Y. Scaling of the anomalous Hall effect in perpendicularly magnetized epitaxial films of the ferrimagnet NiCo_2O_4 . *Phys. Rev. B* **104**, 134407 (2021).
51. Park, G.-H. *et al.* Thickness dependence of the anomalous Nernst effect and the Mott relation of Weyl semimetal Co_2MnGa thin films. *Phys. Rev. B* **101**, 060406 (2020).
52. Lu, Y. M., Cai, J. W., Guo, Z. & Zhang, X. X. Unconventional scaling of the anomalous Hall effect accompanying electron localization correction in the dirty regime. *Phys. Rev. B* **87**, 094405 (2013).
53. Roy, P. *et al.* Origin of topological Hall-like feature in epitaxial SrRuO_3 thin films. *Adv. Electron. Mater.* **9**, 2300020 (2023).
54. Isogami, S., Masuda, K., Miura, Y., Rajamanickam, N. & Sakuraba, Y. Anomalous Hall and Nernst effects in ferrimagnetic Mn_4N films: Possible interpretations and prospects for enhancement. *Appl. Phys. Lett.* **118**, 092407 (2021).
55. Duijn, H. G. M., Bruck, E., Buschow, K. H. J., de Boer, F. R. & Coehoorn, R. Magnetic and transport properties of $\text{Fe}_3(\text{Ga}_{1-x}\text{Al}_x)_4$ compounds. *Physica B* **245**, 195–200 (1998).
56. Hirschberger, M. *et al.* Skyrmion phase and competing magnetic orders on a breathing kagomé lattice. *Nat. Commun.* **10**, 5831 (2019).
57. Thessieu, C., Pfeleiderer, C., Stepanov, A. N. & Flouquet, J. Field dependence of the magnetic quantum phase transition in MnSi . *J. Phys.: Condens. Matter* **9**, 6677 (1997).
58. Takagi, R. *et al.* Square and rhombic lattices of magnetic skyrmions in a centrosymmetric binary compound. *Nat. Commun.* **13**, 1472 (2022).
59. Wang, Q., Sun, S., Zhang, X., Pang, F. & Lei, H. Anomalous Hall effect in a ferromagnetic Fe_3Sn_2 single crystal with a geometrically frustrated Fe bilayer kagome lattice. *Phys. Rev. B* **94**, 075135 (2016).
60. Chen, T. *et al.* Anomalous transport due to Weyl fermions in the chiral antiferromagnets Mn_3X , $\text{X} = \text{Sn, Ge}$. *Nat. Commun.* **12**, 572 (2021).
61. Soumyanarayanan, A. *et al.* Tunable room-temperature magnetic skyrmions in Ir/Fe/Co/Pt multilayers. *Nat. Mater.* **16**, 898–904 (2017).
62. He, M. *et al.* Evolution of topological skyrmions across the spin reorientation transition in Pt/Co/Ta multilayers. *Phys. Rev. B* **97**, 174419 (2018).
63. Mourkas, A., Markou, A., Swekis, P. & Panagiotopoulos, I. Topological Hall effect in Pt/Co/W multilayers with different anisotropies. *J. Magn. Magn. Mater.* **530**, 167937 (2021).
64. Raju, M. *et al.* The evolution of skyrmions in Ir/Fe/Co/Pt multilayers and their topological Hall signature. *Nat. Commun.* **10**, 696 (2019).
65. Mohanty, S., Ojha, B., Sharma, M. & Bedanta, S. Observation of topological Hall effect and skyrmions in Pt/Co/Ir/Co/Pt system. *Mater. Res. Express* **11**, 046406 (2024).
66. Khanh, N. D. *et al.* Nanometric square skyrmion lattice in a centrosymmetric tetragonal magnet. *Nat. Nanotechnol.* **15**, 444 (2020).
67. Neubauer, A. *et al.* Topological Hall effect in the A phase of MnSi . *Phys. Rev. Lett.* **102**, 186602 (2009).
68. Zeissler, K. *et al.* Discrete Hall resistivity contribution from Néel skyrmions in multilayer nanodiscs. *Nat. Nanotechnol.* **13**, 1161–1166 (2018).
69. Wang, L. *et al.* Ferroelectrically tunable magnetic skyrmions in ultrathin oxide heterostructures. *Nat. Mater.* **17**, 1087–1094 (2018).
70. Vistoli, L. *et al.* Giant topological Hall effect in correlated oxide thin films. *Nat. Phys.* **15**, 67–72 (2019).
71. Romming, N. *et al.* Writing and deleting single magnetic skyrmions. *Science* **341**, 636–639 (2013).
72. Pollard, S. D. *et al.* Observation of stable Néel skyrmions in cobalt/palladium multilayers with Lorentz transmission electron microscopy. *Nat. Commun.* **8**, 14761 (2017).
73. Barthel, J. Dr. Probe: A software for high-resolution STEM image simulation. *Ultramicroscopy* **193**, 1–11 (2018).

Acknowledgments

We thank Xiaodong Zhou for fruitful discussions. This work was supported by the National Natural Science Foundation of China (Grant Nos. 12374105 and 12350710785), the Natural Science Foundation of Shanghai (Grant Nos. 21ZR1420500 and 21JC1402300), the Natural Science Foundation of Chongqing (Grant No. CSTB-2022NSCQ-MSX1678), and the Fundamental Research Funds for the Central Universities. J.M. acknowledges the financial support from the National Natural Science Foundation of China (Grant Nos. U2032213 and 12334008).

Author contributions

T.Sha. and Q.Z. conceived and led the project. J.Me. and D.J.G. synthesized the sample. Z.Y. and Y.S. performed the scanning transmission electron microscopy measurements. K.Z. and H.W. fabricated the devices. H.Y. performed the magnetic force microscopy measurements. J.Me., Y.W., K.X., B.Y., X.Z., B.L., Y.H., J.Ma., and Y.X. performed the magnetization and electrical transport measurements. J.Me. and H.Y. analyzed the experimental data. J.Me., T.Shi., Q.Z., and T.Sha. wrote the paper with input from all authors.

Conflict of interest

The authors declare no competing interests.

Additional information

Supplementary information The online version contains supplementary material available at <https://doi.org/xxxxx>.